ELSEVIER

Contents lists available at ScienceDirect

Additive Manufacturing

journal homepage: www.elsevier.com/locate/addma





Assisted defect detection by in-process monitoring of additive manufacturing using optical imaging and infrared thermography

Youssef AbouelNour*, Nikhil Gupta

Composite Materials and Mechanics Laboratory, Mechanical and Aerospace Engineering Department, New York University, Tandon School of Engineering, 6 MetroTech Center, Brooklyn, NY 11201 USA

ARTICLE INFO

Keywords:
Additive manufacturing
In-process monitoring
Defect detection
Thermal imaging
Optical imaging

ABSTRACT

Layer-wise in-process monitoring in Fused Filament Fabrication (FFF) 3D printing can facilitate the detection of defects introduced during manufacturing. In this work, optical imaging and infrared (IR) thermography were used simultaneously for the detection of embedded defects, such as point and line defects. The optical images helped in identifying the necessary variables that can lead to real-time defect detection through image correlation. Through temperature monitoring and thermal image analysis, defect detection was accomplished by comparing to a baseline. It was found that as the number of embedded defects increased in a specimen, the average specimen temperature, $\tilde{T}_{specimen}$, increased. An increase in the number of defects by 2X and 5X led to an increase in $\tilde{T}_{specimen}$ that is \sim 18X and 37X the relative standard error. There was also a positive correlation between the global average hotspot temperature, $\tilde{T}_{hotspot}$, and the total number of embedded defects in the specimen. This study demonstrates that in-situ defect detection can be accomplished using optical and thermal imaging systems.

1. Introduction

Additive Manufacturing (AM) processes are affected by a vast number of user-defined parameters, as well as many external variables that affect the quality of the print [1]. Non-destructive testing (NDT) methods such as micro-CT scan are now extensively used for characterizing the defects in AM specimens [2–4]. Although detection of defects in a finished part provides valuable quality information, in-process monitoring of part manufacturing provides possibility of intervention or repair so that the print can be salvaged. These in-situ NDT procedures can accomplish defect detection and process control and help in understanding the effects of process parameters on build quality [5]. The effects of manufacturing defects on mechanical behaviors of printed polymer parts has been studied in great detail [6,7]. However, real-time detection of size, location and orientation of defects can also help in assessing their impact on mechanical properties of the part and assist in reducing material wastage, build time, and resource consumption [8,9].

Simultaneous use of multiple optical sensors for monitoring AM prints requires development of an optical system, which can be on-axis, off-axis, or coaxial [10–13]. The spatial resolution of an optical system can be improved by increasing camera resolution, fine-tuning sensor

position, and adjusting field of view (FOV) [14,15]. As a result, the validity of acquired datasets and experimental results can be improved [13,16,17]. Several works have shown the possibility of real-time defect detection using optical and thermal imaging cameras [5,18–26]. These publications have laid the foundation for this work by providing direction on the development of in-situ monitoring systems and analysis of acquired data. In other studies, image processing techniques have been established to assist with defect detection using optical cameras [27]. Abnormalities have been detected using edge detection filters for optical image processing, which will also be an approach in this work [28–31]. The development of defect correction strategies, however, remains scarce. Use of a digital twin for verification and validation may serve as a quality index and may also allow automatic intervention and defect correction in-situ [32].

Research studies on FFF have used optical and thermal cameras for extruder state monitoring, temperature monitoring, and abnormalities and error detection [5,27,33–35]. This has been accomplished with both stationary and kinetic monitoring systems. The utilization of acquired thermal data for defect detection purposes remains a topic of concern. In one study with a multi-sensor kinetic monitoring system, infrared (IR) thermal sensors were used to identify temperature deviations caused by

E-mail address: ywa201@nyu.edu (Y. AbouelNour).

^{*} Corresponding author.

intentionally embedded defects in an FFF print [36]. Voids as small as 1.5 mm in width and over-extrusion defects were detected using the two IR sensors. In this work, a multi-sensor stationary monitoring system is uniquely installed and used to acquire data using simultaneous camera-based optical testing and IR thermography for real-time defect detection in an FFF process. The work combines temperature variations monitoring and a novel approach of abnormalities detection for the purpose of defect detection by comparing to a baseline. Random point and line defects are intentionally embedded in the G-code as voids using an algorithm. In-situ monitoring methods for image acquisition are introduced. Image analysis methods are used to detect abnormalities and a novel in-situ assisted defect detection strategy is developed through thermal imaging analysis. In the proposed approach, compromised AM prints are detected in-situ through the acquired raw dataset by creating a snapshot of temperature variations at a specific time stamp for each layer of the print.

2. Materials and methods

2.1. Layer slicing using Ultimaker Cura

A CAD model of the ASTM D638 standard dog-bone specimen was created using SolidWorks and imported into Ultimaker Cura 4.9.1 for slicing. Printing process parameters were kept the same for all specimens. Layer height and print speed were set to 0.2 mm and 80 mm/s, respectively. Default settings were applied in Cura for other parameters such as walls, infill, extruder travel, and material flow and temperature. A three-layer raft was created to avoid warping. Using the modify G-code extension native to Cura, the timelapse feature was enabled to move the extruder to a specified location after completion of each layer, allowing for a direct line of sight to the deposited layer to acquire images of high quality and consistent position. Pause length was set to 5 s

The specimen was sliced into 33 layers, including the three-layer raft labeled as layers 1–3. Each layer consisted of inner walls, an outer wall, and infill. Fig. 1a demonstrates the printing process for layers 4–7 and 30–33 of the defect-free specimen, while Fig. 1b demonstrates the printing process for layers 8–29.

2.2. G-code adjustments for embedding defects

Dog-bone specimens with several variations of defect patterns were printed for monitoring. Generated G-code files with embedded defects,

or specimen *Types*, were named alphabetically, ranging from *Type A* to *Type F*. Defects were seeded in the part by altering the extrusion pattern to create voids and delay extrusion commands while keeping the specimen weight unchanged. This modification takes place every α number of cycles or number of lines of G-code, where α is an integer that decreases in value from *Types A* through *F*, which implies that the total number of defects increases in that order. Defects were not seeded in the first and last 25% of the print to ensure only invisible internal defects.

Moreover, the frequency of adjustments and location of defects varies from layer to layer and from type to type due to the correlation between α and the size of a G-code file. Depending on the defects' locations in the G-code and due to the nature of printing pattern and extruder movement in any layer of the print (see Figs. 1a and 1b), it was later discovered that there are two types of defects that can be created in *Types A* through *F*. The first type of defect is a void that is formed on either the inner walls or outer wall of a layer. The sizes of these voids fall into two different ranges. For analysis purposes, these voids will be classified as either point defects (~ 1 mm in length) or line defects (≥ 30 mm in length). The second type of defect is the lack of extrusion of an infill line. The type of defect that occurs varies depending on α , as α ultimately decides the frequency of defect formation, and hence, the specific position of a defect in any particular layer.

To determine the value of α for each type, a script was written in Python. G-code files were input into the script and analyzed to determine the number of modifications that were made, or defects embedded, for each type. It was confirmed that α decreases from $Type\ A$ through $Type\ F$, with values of 20, 10, 8, 5, 4, and 3, respectively. The number of defects found to exist in each type are shown in Table 1.

Table 1 Frequency of defect formation, α , and total number of embedded defects in *Types A-F*.

Туре	α	# of Defects
A	20	146
В	10	297
C	8	369
D	5	593
E	4	736
F	3	982

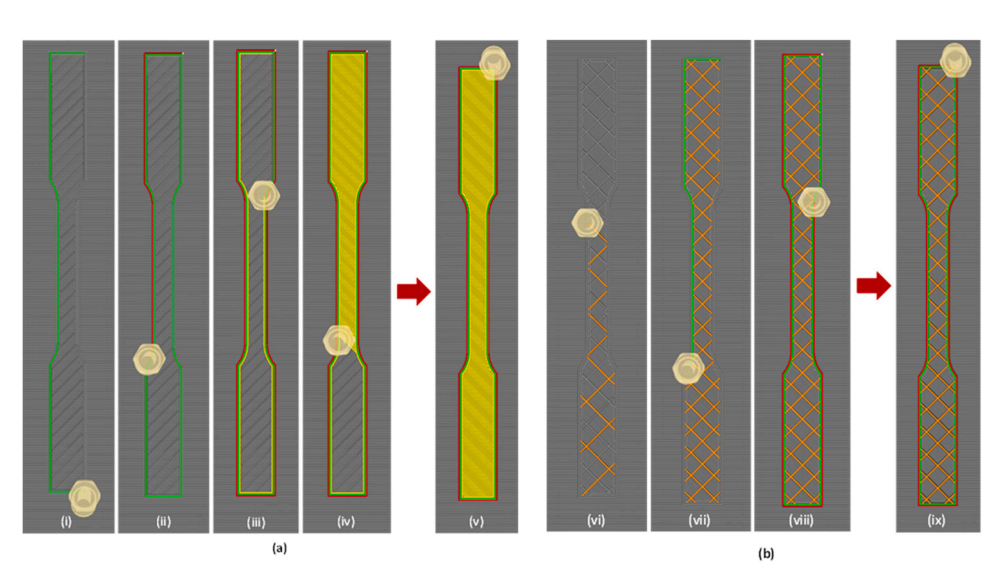


Fig. 1. Typical sequence of extruder movement for formation of (a) layers 4–7 and 30–33 of the printed specimen: (i) inner wall #1 in green, (ii) outer wall in red, (iii) inner wall #2 in yellow, (iv) infill, and (v) complete layer with final extruder position, and (b) layers 8–29: (vi) infill in orange, (vii) inner wall in green, (viii) outer wall in red, and (ix) complete layer with final extruder position.

2.3. Visual inspection of models

Inspection of the sliced models allowed for a clearer understanding of defect formation in the printed specimens, which helped to thoroughly analyze the acquired in-situ monitoring data. Fig. 2 shows the different types of defects that can form in $Types\ A$ through F. They consist of voids of different sizes and missing infill lines. The variation in the spatial location of defects is evident, which is expected to pose a challenge in their detection.

It was found that no defects were present in the first 5 layers and last 7 layers of the print. Further analysis of sliced layers of *Types A-F* with a focus on the frequency and locations of point defects led to the conclusion that the majority of these defects were formed at the fillets in the inner and outer walls. Other major locations with the greatest number of point defects were at the four corners of the specimen in both the inner and outer walls (see Fig. 3 for locations of corners and fillets). Table 2 assigns numbers to different combinations of point defects at the inner and outer walls, where *fillet* refers to the specimen's four fillets (see Fig. 3) and *throughout* refers to all corners (4) and fillets (4) in the specimen. Combinations are then assigned to each of the six specimen types. Table 2 shows that voids at the fillets increased from *Types A* through *F*. This can also be seen in Fig. 4, where the number of voids, or point defects, at the fillets increased from *Type A* to *C* to *F*.

Fig. 5 shows that the number of line defects also increased from *Type A* to *C* to *F*. These line defects, or pauses in material extrusion along the inner and outer walls, ranged from the fillet to the next adjacent corner of the specimen. Defects that occurred in the infill due to a lack of extrusion of infill lines (defect type 2) could not be clearly depicted in Cura, however. This is due to the nature of the raster pattern, where the overlap of infill lines in deposited layers obscures the absence of any single infill line in the stack.

Inspection of the sliced model served as a guide to analyze the in-situ monitoring data, which may be evolved into further use of a digital twin for assisted defect detection. Nonetheless, the procedures and techniques presented in this work can be replicated for other experiments where the frequencies and locations of defects are unknown.

2.4. In-situ monitoring and image acquisition

An off-axis multi-sensor monitoring system was developed, consisting of an IR thermal imaging camera and an optical camera mounted on

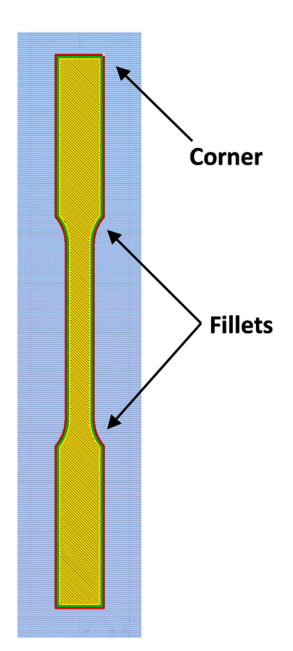


Fig. 3. Locations of fillets and corners on ASTM dog-bone specimen.

a Prusa MK3 3D Printer. All specimens were printed using polylactic acid (PLA).

A GoPro Hero 8 Black 12 MP CMOS Camera was used for optical imaging due to its desirable resolution, design, and image acquisition frequency. The camera offers an Auto mode capable of capturing up to 30 photos/s. In addition, an IR camera (FLIR E5-XT) was integrated into the monitoring setup to capture thermal images. It acquires radiometric images at a frequency of 9 Hz and resolution of 19,200 (160 $\times 120$) pixels with a spectral range of $7.5-13~\mu m$, an extended temperature range of $-4-752^{\circ} F$, and a resolution of $0.001^{\circ} F$. The FLIR camera is capable of capturing both thermal and optical images, as well as producing fused images using its proprietary technology, FLIR MSX®, or the Multi-Spectral Dynamics Imaging tool. This tool is capable of capturing key elements of optical images such as outlines, edges, words, and numbers, and overlaying them onto the thermal images.

Two different monitoring setups were used in the experiments. In the first setup, Fig. 6a, the optical camera was mounted on the outer frame

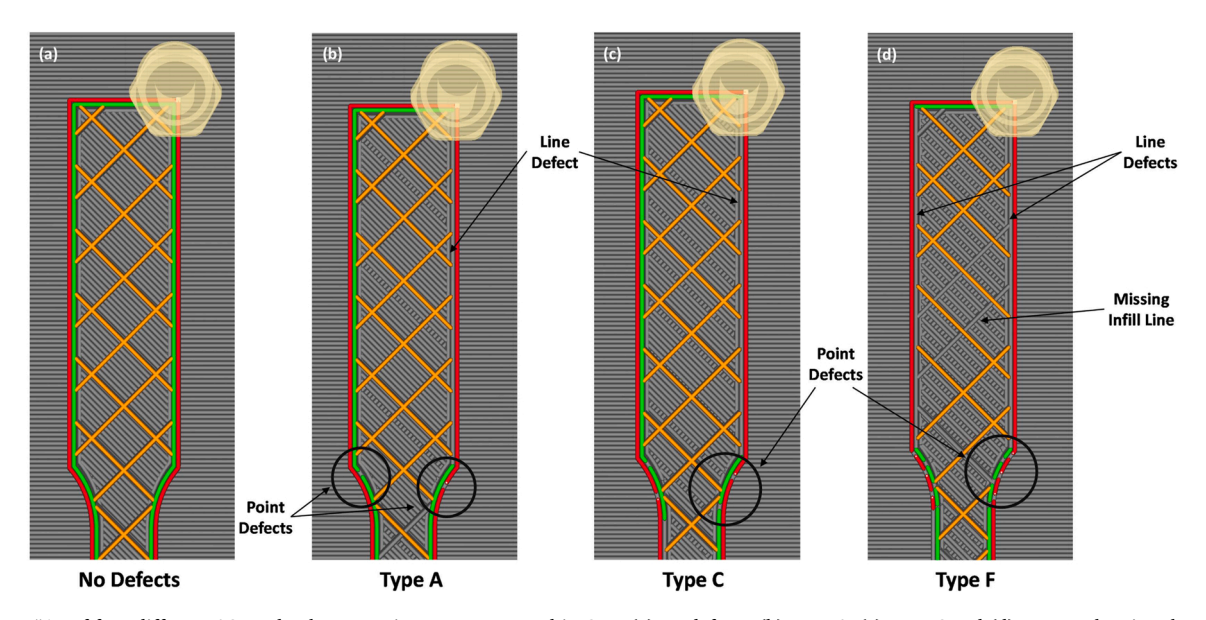


Fig. 2. Layer #15 of four different ASTM dog-bone specimens as presented in Cura (a) no defects, (b) *Type A*, (c) *Type C* and (d) *Type F*, showing the variation in defects across specimens and the increasing number of defects from *Type A* to *Type F*.

Table 2 Assigned numbers for the combinations of point defects in the inner and outer walls for *Types A-F*.

Inner Wall (Green) 2/3 voids @ fillets 2 voids @ fillets 2 voids @ fillets 3 voids throughout 2 voids @ fillets 5 voids throughout 2 voids @ fillets 5 voids throughout 2 voids @ fillets 5 voids throughout 4 voids @ fillets 5/6 voids throughout 4 voids @ fillets 7 8 voids throughout 4 voids @ fillets 5 voids throughout 4 voids @ fillets 7 8 voids throughout 4 voids @ fillets 9 voids throughout 10 5 voids @ fillets 6 voids @ fillets 6 voids @ fillets 9 voids @ fillets 11 8 voids @ fillets 5 voids @ fillets 11 8 voids @ fillets 6 voids throughout 10 5 voids @ fillets 6 voids throughout 11 7 voids throughout 5 voids @ fillets 13 6 voids throughout 6 /7 voids @ fillets 13 6 voids throughout 6 /7 voids @ fillets 14 6 voids throughout 15 7 voids @ fillets 6 voids throughout 11 12 voids throughout 16 8 voids @ fillets 9 voids throughout 16 8 voids @ fillets 9 voids throughout 11 voids throughout 12 voids throughout 13 voids throughout 14 voids throughout 15 12 voids throughout 11 voids throughout 12 voids throughout 13 voids throughout 14 voids throughout 11 voids throughout 11 voids throughout 12 voids throughout 11 voids throughout 12 voids throughout 11 voids throughout 12 voids throughout 13 voids throughout 14 voids throughout 15 13/14 voids throughout 13 voids throughout 14 voids throughout 15 15 voids throughout 17 voids throughout 17 voids throughout 18 18 19 13/14 voids throughout 11 voids throughout 22 11 voids throughout 11 voids throughout 23 13/14 voids throughout 12 voids throughout 24 15 voids throughout 17 voids throughout 27 15 voids throughout 17 voids throughout 27 17	Combination		A : 137 1	_
2 voids @ fillets 4/5 voids throughout 2 3 voids throughout 2 voids @ fillets 3 5 voids throughout 2 voids @ fillets 4 4 voids @ fillets 4-6 voids @ fillets 5 4 voids @ fillets 7/8 voids throughout 6 5/6 voids throughout 4 voids @ fillets 7 8 voids throughout 4 voids @ fillets 8 6 voids @ fillets 4 voids @ fillets 9 4/5 voids @ fillets 5 voids @ fillets 11 8 voids @ fillets 5 voids @ fillets 11 8 voids fhroughout 5/6 voids throughout 12 7 voids (@ fillets 13 6 6 voids throughout 6/7 voids @ fillets 14 C 6 voids throughout 15 7 7 voids @ fillets 9 voids throughout 15 7 voids @ fillets 9 voids throughout 16 8 voids @ fillets 9 voids throughout 17 9 voids throughout 11 voids throughout 18 9 voids throughout 12 voids throug	Inner Wall (Green)	Outer Wall (Red)	Assigned Numbers	Type
3 voids throughout 2 voids @ fillets 3 A 5 voids throughout 2 voids @ fillets 4 4 voids @ fillets 4 4 4 voids @ fillets 7/8 voids throughout 6 5/6 voids throughout 4 voids @ fillets 7 8 voids throughout 4 voids @ fillets 8 6 voids @ fillets 4 voids @ fillets 9 4/5 voids @ fillets 5 voids @ fillets 9 4/5 voids @ fillets 5 voids @ fillets 11 8 voids @ fillets 5 voids @ fillets 11 8 voids fillets 5 voids @ fillets 13 6 voids throughout 5/6 voids throughout 12 7 voids @ fillets 14 C 6 voids throughout 15 7 7 voids @ fillets 9 voids throughout 15 7 voids @ fillets 9 voids throughout 17 9 voids throughout 11 voids throughout 18 9 voids throughout 12 voids throughout 19 12 voids throughout 10 voids throughout				
5 voids throughout 2 voids @ fillets 4 4 voids @ fillets 4-6 voids @ fillets 5 4 voids @ fillets 7/8 voids throughout 6 5/6 voids throughout 4 voids @ fillets 7 8 voids throughout 4 voids @ fillets 8 6 voids @ fillets 4 voids @ fillets 9 4/5 voids @ fillets 6 voids throughout 10 5 voids @ fillets 5 voids @ fillets 11 8 voids throughout 5/6 voids throughout 12 7 voids throughout 5 voids @ fillets 13 6 voids throughout 5 voids @ fillets 13 6 voids throughout 6/7 voids @ fillets 14 6 voids throughout 8 voids throughout 15 7 voids @ fillets 6 voids throughout 15 9 voids (fillets 10 8 voids @ fillets 11 8 voids @ fillets 12 10 voids throughout 15 11 voids (fillets 10 8 voids @ fillets 11 9 voids throughout 11 voids throughout 16 8 voids @ fillets 9 voids throughout 16 9 voids throughout 11 voids throughout 19 10 voids throughout 12 voids throughout 19 12 voids throughout 10 voids throughout 11 13/14 voids throughout 11 voids throughout 22 11 voids throughout 11 voids throughout 23 13/14 voids throughout 12 voids throughout 24 11 voids throughout 12 voids throughout 25 15 voids throughout 17 voids throughout 27 F				
4 voids @ fillets 4-6 voids @ fillets 5 4 voids @ fillets 7/8 voids throughout 6 5/6 voids throughout 4 voids @ fillets 7 8 voids throughout 4 voids @ fillets 8 6 voids @ fillets 4 voids @ fillets 9 4/5 voids @ fillets 5 voids @ fillets 9 4/5 voids @ fillets 5 voids @ fillets 10 5 voids @ fillets 11 8 8 voids @ fillets 5 voids @ fillets 11 8 voids throughout 5/6 voids throughout 12 7 voids throughout 6/7 voids @ fillets 14 C 6 voids throughout 15 7 7 7 voids @ fillets 6 voids throughout 16 8 8 voids @ fillets 9 voids throughout 17 9 voids throughout 11 voids throughout 18 9 9 voids throughout 19 D D 12 voids throughout 10 voids throughout 20 1 12 voids throughout 11 voids throughout 22 <td>U</td> <td>~</td> <td></td> <td>A</td>	U	~		A
4 voids @ fillets 7/8 voids throughout 6 5/6 voids throughout 4 voids @ fillets 7 8 voids throughout 4 voids @ fillets 8 6 voids @ fillets 4 voids @ fillets 9 4/5 voids @ fillets 6 voids throughout 10 5 voids @ fillets 5 voids @ fillets 11 8 voids throughout 5/6 voids throughout 12 7 voids throughout 5 voids @ fillets 13 6 voids throughout 6/7 voids @ fillets 14 C 6 voids throughout 15 7 7 7 7 voids @ fillets 9 voids throughout 15 7 7 7 8 voids @ fillets 9 voids throughout 16 8 8 8 8 C 8 voids throughout 18 9	5 voids throughout	2 voids @ fillets	4	_
5/6 voids throughout 4 voids @ fillets 8 8 voids throughout 4 voids @ fillets 8 6 voids @ fillets 4 voids @ fillets 9 4/5 voids @ fillets 6 voids throughout 10 5 voids @ fillets 5 voids @ fillets 11 8 voids throughout 5/6 voids throughout 12 7 voids throughout 5 voids @ fillets 13 6 voids throughout 6/7 voids @ fillets 14 6 voids throughout 8 voids throughout 15 7 voids @ fillets 6 voids throughout 15 8 voids @ fillets 14 6 voids throughout 8 voids throughout 15 7 voids @ fillets 6 voids throughout 16 8 voids @ fillets 9 voids throughout 17 9 voids throughout 11 voids throughout 18 9 voids throughout 12 voids throughout 19 12 voids throughout 12 voids @ fillets 20 12 voids throughout 10 voids throughout 21 13/14 voids throughout 14 voids throughout 22 11 voids throughout 11 voids throughout 23 13/14 voids throughout 13 voids throughout 24 11 voids throughout 12 voids throughout 25 15 voids throughout 17 voids throughout 27 F	4 voids @ fillets	4-6 voids @ fillets	5	
8 voids throughout 4 voids @ fillets 9 4/5 voids @ fillets 4 voids @ fillets 9 4/5 voids @ fillets 6 voids throughout 10 5 voids @ fillets 5 voids @ fillets 11 8 voids throughout 5/6 voids throughout 12 7 voids throughout 5 voids @ fillets 13 6 voids throughout 6/7 voids @ fillets 14 6 voids throughout 8 voids throughout 15 7 voids @ fillets 6 voids throughout 16 8 voids @ fillets 6 voids throughout 16 8 voids @ fillets 9 voids throughout 17 9 voids throughout 11 voids throughout 18 9 voids throughout 11 voids throughout 19 12 voids throughout 12 voids throughout 19 12 voids throughout 10 voids throughout 21 13/14 voids throughout 11 voids throughout 22 11 voids throughout 11 voids throughout 23 13/14 voids throughout 12 voids throughout 24 11 voids throughout 13 voids throughout 25 15 voids throughout 17 voids throughout 26 17 voids throughout 17 voids throughout 27 F	4 voids @ fillets	7/8 voids throughout	6	
8 voids @ fillets 4 voids @ fillets 9 4/5 voids @ fillets 4 voids @ fillets 9 4/5 voids @ fillets 6 voids throughout 10 5 voids @ fillets 5 voids @ fillets 11 8 voids (fillets 5 voids @ fillets 12 7 voids throughout 5 voids @ fillets 13 6 voids throughout 6/7 voids @ fillets 14 C 6 voids throughout 15 7 15 7 7 voids @ fillets 9 voids throughout 16 8 8 9 16 9 16 9 16 9 16 9 16 9 16 9 16 9 16 9 16 9 16 9 16 9 16 9 16 9 16 9 16 9 17 18 9 17 18 9 18 9 18 9 18 19 19 19 10 10 12 12 12	5/6 voids throughout	4 voids @ fillets	7	
4/5 voids @ fillets 6 voids throughout 10 5 voids @ fillets 5 voids @ fillets 11 8 voids throughout 5/6 voids throughout 12 7 voids throughout 5 voids @ fillets 13 6 voids throughout 6/7 voids @ fillets 14 C 6 voids throughout 15 7 15 7 7 voids @ fillets 6 voids throughout 16 6 16 16 8 voids @ fillets 9 voids throughout 17 9 17 18 9 17 18 19 19 19 10 <	8 voids throughout	4 voids @ fillets	8	В
5 voids @ fillets 5 voids @ fillets 11 8 voids throughout 5/6 voids throughout 12 7 voids throughout 5 voids @ fillets 13 6 voids throughout 6/7 voids @ fillets 14 C 6 voids throughout 15 15 14 C 6 voids throughout 15 15 15 7 16 15 17 10 16 16 16 16 16 16 17 17 17 18 17 18 18 18 18 19 18 19 18 19 18 19 19 19 10 10 12	6 voids @ fillets	4 voids @ fillets	9	
8 voids throughout 5/6 voids throughout 12 7 voids throughout 5 voids @ fillets 13 6 voids throughout 6/7 voids @ fillets 14 6 voids throughout 15 7 voids @ fillets 6 voids throughout 16 8 voids @ fillets 9 voids throughout 17 9 voids throughout 11 voids throughout 18 9 voids throughout 12 voids throughout 19 12 voids throughout 8 voids @ fillets 20 12 voids throughout 10 voids throughout 21 13/14 voids throughout 11 voids throughout 22 11 voids throughout 13 voids throughout 23 13/14 voids throughout 13 voids throughout 24 E 15 voids throughout 17 voids throughout 26 15 voids throughout 17 voids throughout 27 F	4/5 voids @ fillets	6 voids throughout	10	
7 voids throughout 5 voids @ fillets 13 C 6 voids throughout 6/7 voids @ fillets 14 C 6 voids throughout 15 15 7 7 voids @ fillets 6 voids throughout 16 8 8 voids @ fillets 9 voids throughout 17 9 9 voids throughout 11 voids throughout 18 9 9 voids throughout 12 voids throughout 19 D 12 voids throughout 8 voids @ fillets 20 20 12 voids throughout 10 voids throughout 21 13/14 voids throughout 14 voids throughout 22 11 voids throughout 13 voids throughout 23 13/14 voids throughout 13 voids throughout 24 E 15 voids throughout 17 voids throughout 26 F 15 voids throughout 17 voids throughout 27 F	5 voids @ fillets	5 voids @ fillets	11	
6 voids throughout 6/7 voids @ fillets 14 6 voids throughout 8 voids throughout 15 7 voids @ fillets 6 voids throughout 16 8 voids @ fillets 9 voids throughout 17 9 voids throughout 11 voids throughout 18 9 voids throughout 12 voids throughout 19 12 voids throughout 12 voids throughout 20 12 voids throughout 10 voids @ fillets 20 12 voids throughout 10 voids throughout 21 13/14 voids throughout 14 voids throughout 21 11 voids throughout 11 voids throughout 23 13/14 voids throughout 13 voids throughout 24 11 voids throughout 12 voids throughout 25 15 voids throughout 17 voids throughout 26 17 voids throughout 17 voids throughout 27 F	8 voids throughout	5/6 voids throughout	12	
6 voids throughout 6/7 voids @ fillets 14 6 voids throughout 8 voids throughout 15 7 voids @ fillets 6 voids throughout 16 8 voids @ fillets 9 voids throughout 17 9 voids throughout 11 voids throughout 18 9 voids throughout 12 voids throughout 19 12 voids throughout 12 voids throughout 20 12 voids throughout 10 voids @ fillets 20 12 voids throughout 10 voids throughout 21 13/14 voids throughout 14 voids throughout 21 11 voids throughout 11 voids throughout 23 13/14 voids throughout 13 voids throughout 24 11 voids throughout 12 voids throughout 25 15 voids throughout 17 voids throughout 26 17 voids throughout 17 voids throughout 27 F	7 voids throughout	5 voids @ fillets	13	
7 voids @ fillets 6 voids throughout 16 8 voids @ fillets 9 voids throughout 17 9 voids throughout 11 voids throughout 18 9 voids throughout 12 voids throughout 19 D 12 voids throughout 8 voids @ fillets 20 20 12 voids throughout 10 voids throughout 21 13/14 voids throughout 14 voids throughout 22 11 voids throughout 11 voids throughout 23 13/14 voids throughout 13 voids throughout 24 E 11 voids throughout 12 voids throughout 25 E 15 voids throughout 17 voids throughout 26 F 17 voids throughout 17 voids throughout 27 F	ě .	6/7 voids @ fillets	14	C
7 voids @ fillets 6 voids throughout 16 8 voids @ fillets 9 voids throughout 17 9 voids throughout 11 voids throughout 18 9 voids throughout 12 voids throughout 19 D 12 voids throughout 8 voids @ fillets 20 20 12 voids throughout 10 voids throughout 21 21 13/14 voids throughout 14 voids throughout 22 22 11 voids throughout 11 voids throughout 23 23 13/14 voids throughout 13 voids throughout 24 E 11 voids throughout 12 voids throughout 25 E 15 voids throughout 17 voids throughout 26 F 17 voids throughout 17 voids throughout 27 F	6 voids throughout	8 voids throughout	15	
9 voids throughout 11 voids throughout 18 9 voids throughout 12 voids throughout 19 12 voids throughout 8 voids @ fillets 20 12 voids throughout 10 voids throughout 21 13/14 voids throughout 14 voids throughout 22 11 voids throughout 11 voids throughout 23 13/14 voids throughout 13 voids throughout 24 11 voids throughout 12 voids throughout 25 15 voids throughout 17 voids throughout 26 17 voids throughout 17 voids throughout 27 F	7 voids @ fillets	•	16	
9 voids throughout 11 voids throughout 18 9 voids throughout 12 voids throughout 19 12 voids throughout 8 voids @ fillets 20 12 voids throughout 10 voids throughout 21 13/14 voids throughout 14 voids throughout 22 11 voids throughout 11 voids throughout 23 13/14 voids throughout 13 voids throughout 24 11 voids throughout 12 voids throughout 25 15 voids throughout 17 voids throughout 26 17 voids throughout 17 voids throughout 27 F	8 voids @ fillets	9 voids throughout	17	
9 voids throughout 12 voids throughout 19 12 voids throughout 8 voids @ fillets 20 12 voids throughout 10 voids throughout 21 13/14 voids throughout 11 voids throughout 22 11 voids throughout 11 voids throughout 23 13/14 voids throughout 13 voids throughout 24 11 voids throughout 12 voids throughout 25 15 voids throughout 17 voids throughout 26 17 voids throughout 17 voids throughout 27 F	_	•	18	
12 voids throughout 8 voids @ fillets 20 12 voids throughout 10 voids throughout 21 13/14 voids throughout 14 voids throughout 22 11 voids throughout 11 voids throughout 23 13/14 voids throughout 13 voids throughout 24 E 11 voids throughout 12 voids throughout 25 15 voids throughout 17 voids throughout 26 17 voids throughout 17 voids throughout 27	9 voids throughout	12 voids throughout	19	D
13/14 voids throughout 14 voids throughout 22 11 voids throughout 11 voids throughout 23 13/14 voids throughout 13 voids throughout 24 E 11 voids throughout 12 voids throughout 25 15 voids throughout 17 voids throughout 26 17 voids throughout 17 voids throughout 27	ě .		20	ь
11 voids throughout 11 voids throughout 23 13/14 voids throughout 13 voids throughout 24 11 voids throughout 12 voids throughout 25 15 voids throughout 17 voids throughout 26 17 voids throughout 17 voids throughout 27 F	12 voids throughout	10 voids throughout	21	
11 voids throughout 11 voids throughout 23 13/14 voids throughout 13 voids throughout 24 11 voids throughout 12 voids throughout 25 15 voids throughout 17 voids throughout 26 17 voids throughout 17 voids throughout 27 F	13/14 voids throughout	14 voids throughout	22	
13/14 voids throughout 13 voids throughout 24 E 11 voids throughout 12 voids throughout 25 15 voids throughout 17 voids throughout 26 17 voids throughout 17 voids throughout 27 F F	ū		23	
11 voids throughout 12 voids throughout 25 15 voids throughout 17 voids throughout 26 17 voids throughout 17 voids throughout 27 F	13/14 voids throughout	13 voids throughout	24	E
17 voids throughout 17 voids throughout 27 F				
17 voids throughout 17 voids throughout 27 F	15 voids throughout	17 voids throughout	26	
o o	e e		27	F
10 voius unougnout 10 voius unougnout 20	18 voids throughout	16 voids throughout	28	

of the 3D printer. The camera was fastened to an arm extension clipped to the printer. The camera lens was pointed downwards, towards the center of the build plate, and the gridlines on the camera's screen were aligned with those on the printer's build plate. The IR camera was mounted onto a flexible stand and positioned to point downward at the build plate, aligned with the printer's *y*-direction belt. To determine the distance between the IR camera and the build plate, FLIR's online database was used to calculate the FOV of the E5-XT camera. This FOV coincided with that of the optical camera to allow for ease of data correlation and image overlaying.

In the second monitoring setup, Fig. 6b, the optical camera was mounted to the side of the printer using an arm extension attached to the printer using an adhesive. The position of the IR camera remained the same. External lighting was added to the setup to eliminate glare and acquire better quality images.

The second setup provided images with reduced noise at both ends of the specimen. Additionally, it was found that the high-definition macro lens optical camera attachment (minimum focus distance of 100 mm), pictured in Fig. 6a, provided more detailed images at the short depth of field and corrected for the optical camera's default fisheye lens.

Throughout the printing process, the print bed and nozzle were maintained at constant temperatures of $140^{\circ}F$ and $410^{\circ}F$, respectively. Factory calibration of the IR camera's temperature accuracy was confirmed by measuring the print bed temperature. This ensured that the captured thermal images represented accurate emissivity measurements and reflected actual temperature distributions in the build area.

The thermal emissivity of the monitored part needs to be known to achieve absolute temperature measurements via IR imaging [37]. This coefficient is difficult to determine due to the physical transformations that the material undergoes during the AM process. The emissivity of the specimens can be affected by several factors, such as temperature, surface finish, moisture content, chemical composition, and part thickness. The material composition and moisture content are constant during testing. Thin films show different behavior compared to bulk sections. The present case resembles bulk specimens. Hence, temperature is the major contributor in the IR imaging. The calibration was conducted considering the emissivity of the material in its solid-state form [37]. For PLA, the emissivity was determined to be 0.95 [38]. The reflected apparent temperature was set to 68°F.

Both optical and thermal images were captured at the same instant and the images were stored in both JPEG and RAW formats. The spatial resolution of the in-situ monitoring system was determined to be < 1 mm through extensive experiments. Five trial runs were conducted to assess the reliability of the experimental procedure. Both the printer and the monitoring setup were calibrated upon system startup and prior to each new trial run by adjusting each camera's position and angle to maintain consistency and repeatability of the experiment. Optical images were processed and analyzed using ImageJ software [39].

2.5. Image processing

2.5.1. Optical image analysis

During the in-situ monitoring process, the optical camera captured images of the entire build plate, which were then cropped to retain only the printed specimens. This also reduced image size and improved further processing times. A macro was written in ImageJ to automatically crop and save the JPEG images in a new folder. As pictured in Fig. 7, images were reduced in size from 4000×3000 pixels to 375×1659 pixels. File size was reduced from 46 MB to 2.4 MB. Cropped images were then processed to improve brightness and contrast followed by background subtraction and color thresholding. Then, colocalization analyses and other comparison methods based on image feature extraction were performed.

Image analysis for edge detection can facilitate defect detection through comparison of size information, such as perimeter or surface area, for both defect-free and defective specimens. It can also help in understanding discontinuities in the depth of a layer. Several different filters available in ImageJ can be used for edge detection, such as the Sobel filter (used by ImageJ to establish the *Find Edges* algorithm), the Canny filter, and the Laplacian filter [40–43]. A Laplacian filter is a finite impulse response (FIR) filter used as a first-order approximation to the Laplacian of an underlying continuous-space function $x(t_1, t_2)$ [40]:

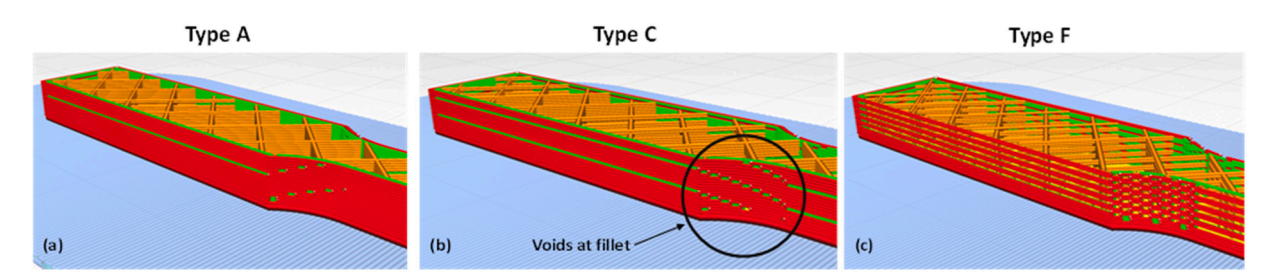


Fig. 4. Section views of three different ASTM dog-bone specimens as presented in Cura (a) Type A, (b) Type C, and (c) Type F, showing increasing number of point defects at fillets.

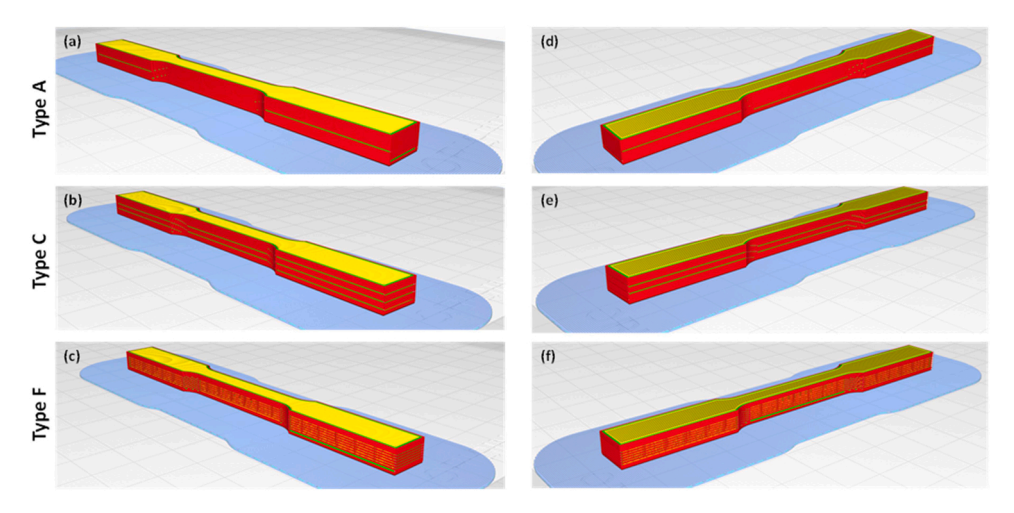


Fig. 5. Isometric views of three different ASTM dog-bone specimens as presented in Cura (a, d) Type A, (b, e) Type C, and (c, f) Type F, showing line defects across the outer walls.

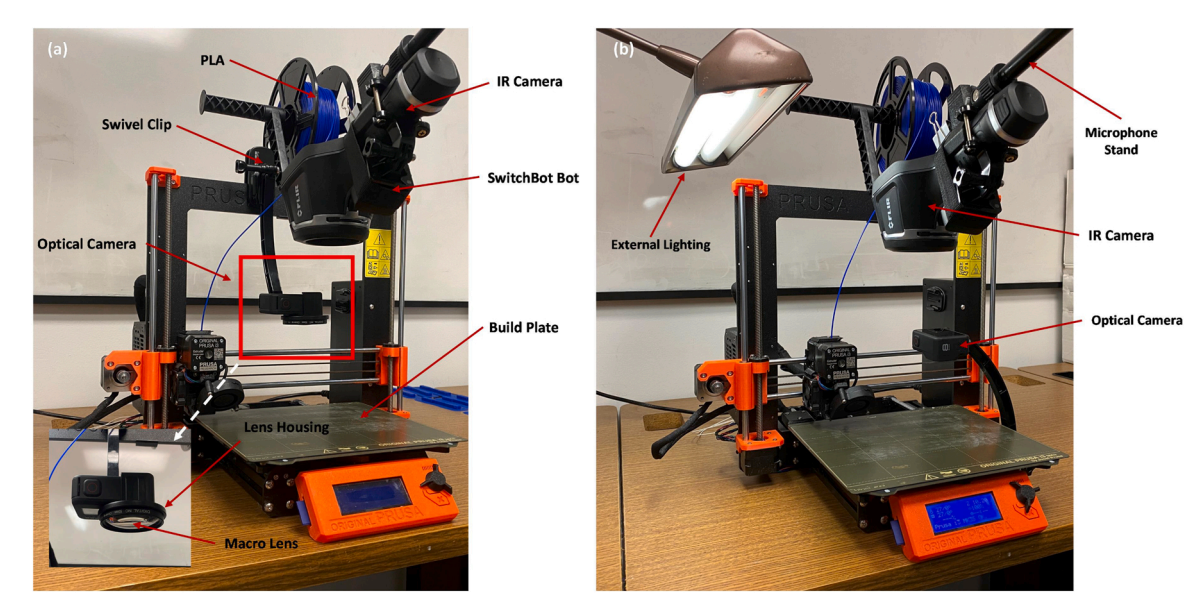


Fig. 6. Off-axis monitoring system consisting of an IR camera with a SwitchBot attachment mounted on a microphone stand and an optical camera with a macro lens attachment installed via a lens housing (a) mounted to the top frame of the 3D printer using a swivel clip and arm extension and (b) mounted to the side of the 3D printer using an arm extension and adhesive.



Fig. 7. Optical image (a) as acquired by the optical camera and (b) cropped using ImageJ.

$$\nabla^2 x(t_1, t_2) = \frac{\partial^2 x(t_1, t_2)}{\partial^2 t_1} + \frac{\partial^2 x(t_1, t_2)}{\partial^2 t_2}$$
 (1)

The Laplacian provides an isotropic measure of the 2nd spatial derivative of an image. The Laplacian of an image can be used for edge detection as it emphasizes regions with large discrepancies in intensity [44]. A smoothing scale, or filter, can be applied prior to use of the Laplacian filter to reduce sensitivity to noise and minimize gray-level difference among neighboring pixels [40]. The smoothing scale acts as a low-pass filter, while the Laplacian filter acts as a high-pass filter [40].

Several factors that affect the image comparison methods used for defect detection include the location of the printed sample relative to the build plate, frequency of image acquisition, and temporal resolution of the monitoring system. Sample size, number of layers, and print duration are all variables that affect frequency of image acquisition due to the cooling cycle following material deposition. For this work, images were acquired within 2 s after completion of a layer. Apart from the raft (\sim 657 s), layers 4–7 (\sim 72 s each), and layers 30–33 (\sim 71 s each), all other layers (8–29) registered about 22.7 s each of elapsed time.

Acquiring one image per layer was sufficient to capture accurate image features and thermal information for image analyses.

2.5.2. Thermal image analysis

Acquired thermal images were processed and analyzed using FLIR Thermal Studio Pro for color gradient adjustment, fusion alignment, and isotherm management, as well as temperature measurements (i.e., reflected, atmospheric, reference), spatial measurements, object distance, and emissivity measurement and adjustment. Analysis showed that elevated temperatures were located at eight different locations on the specimens as indicated in Fig. 3 - each of the four corners and fillets of the specimen - locations at which point defects were embedded in the specimens. Fig. 8 shows images of layers from each of the six specimen types: layers 15, 19, 24, 12, 26, and 10, for Types A through F, respectively. The hotspots were observed at 2 or more of the eight locations for a variety of layers in each of Types A through F. The temperatures of these particular hotspots in the images ranged from \sim 132–168 $^{\circ}$ F. Here, a *hotspot* is identified as a spotmeter measurement greater than or equal to 133°F because of the separation of colors (i.e., blue to green) in the specimens at this temperature.

Spotmeter temperature measurements were taken at these eight locations shown in Fig. 8 and marked as Sp1, Sp2..., Sp8. For the first task, using the *Batch Processing* tool on FLIR Thermal Studio Pro, algorithms were created to take spotmeter measurements on defined locations Sp1-Sp8 for each thermal image in a given trial. Each algorithm consisted of 11 steps as shown in Fig. 9.

The output of each algorithm was a folder with 33.csv files, one for each processed thermal image. Each file contained temperature measurements at the defined locations Sp1-Sp8. For Task 2, Python was used to create a script that reads the.csv files and exports the measurements to an external.csv file to complete the steps listed in Fig. 10.

As mentioned in *Task 2 Step 4*, in addition to $\widetilde{T}_{specimen}$, the output.csv file was also used to determine the total number of hotspots per specimen type and per layer. A correlation was then made between the total number of hotspots and embedded defects in the specimen. Furthermore, to eliminate any bias in comparison, other threshold temperature values were considered: 130, 131, and 132°F. For this correlation, the end condition was considered – 22 layers were evaluated – as to eliminate any layers with elevated spot temperature values.

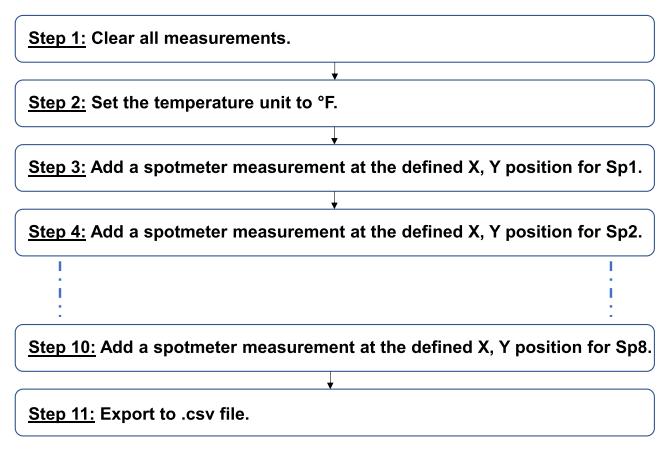


Fig. 9. Batch processing algorithm created in FLIR Thermal Studio Pro.

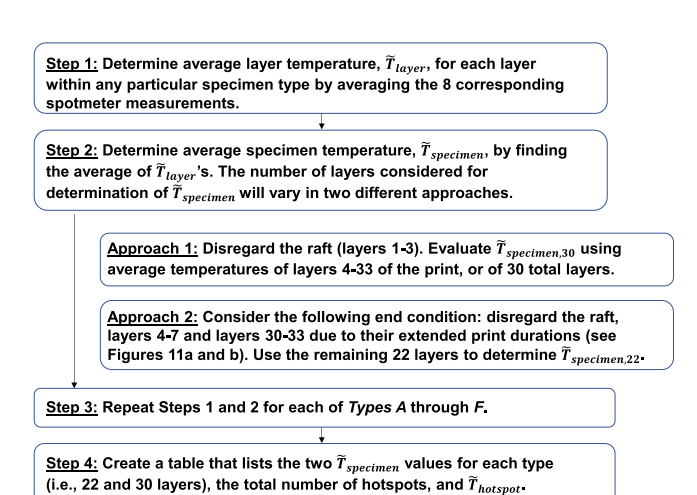


Fig. 10. Steps in python script for determination of $\widetilde{T}_{specimen}$, total number of hotspots, and $\widetilde{T}_{hotspot}$.

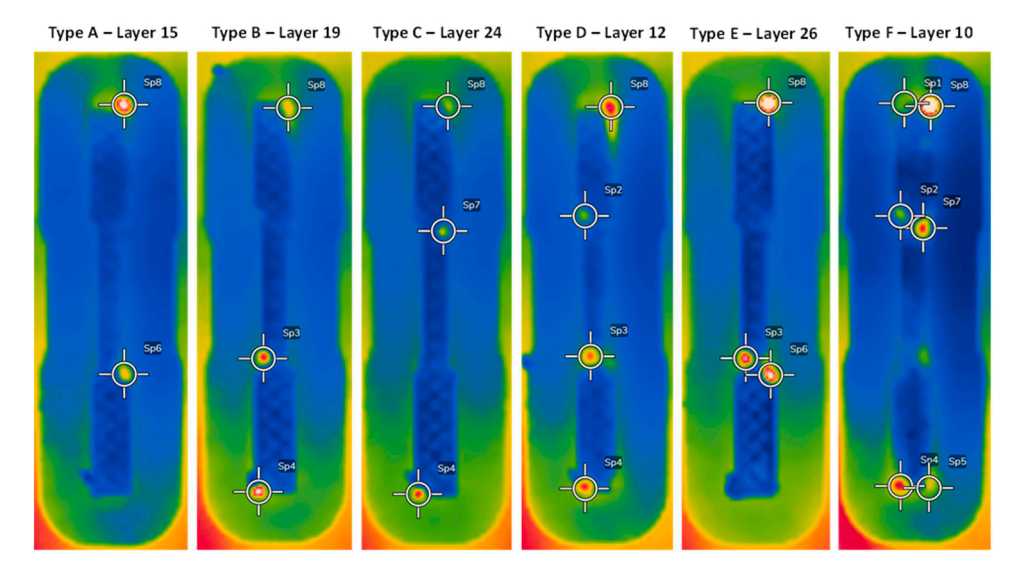


Fig. 8. Thermal images of a variety of layers in each of *Types A* through *F* showing hotspots at two or more of the eight locations where point defects were embedded in the specimens.

3. Results

Large surface defects such as misalignments, over-extrusion, under-extrusion, oozing and incomplete walls are visible in the optical images. Thermal image analysis was used to determine the location of defects by examination of temperature profiles. Locations Sp1-Sp8 could be clearly identified as ones with discrepancies in temperature profiles, or hot-spots. Optical images provided additional detail that could not be seen in thermal images. Events leading up to defect formation can be identified by comparing the temporal evolution of information in the images with the baseline dataset. Results from optical and thermal imaging analyses are presented in this section. (Fig. 11).

First, the processed optical images are compared with the representation of the corresponding layers in Cura files to identify many of the defects. The locations of defects in the images coincided with those in the sliced layers. Furthermore, the accumulation of point defects, such as those in Fig. 12b and c, at the same locations on subsequent layers caused multilayer defects that were apparent as over-extrusions in the optical images, as pictured in Fig. 12a.

Analysis of thermal images allowed for characterization of specimens based on $\widetilde{T}_{specimen}$ and the presence of hotspots in thermal images of the printed layers. Air, with a thermal conductivity of 2.6–6.7 \times 10^{-2} W m $^{-1}$ K $^{-1}$ transfers heat at a lower rate compared to PLA, which has a thermal conductivity of 16.0 \times 10^{-2} W m $^{-1}$ K $^{-1}$ [45]. Therefore, due to the low thermal conductivity of air, entrapped air in the cavities leads to heat retention within the formed voids. This results in elevated temperatures, or hotspots, at locations of void formation.

First, using the procedure mentioned in Section 2.5.2 , $\widetilde{T}_{specimen}$ of Types A-F were determined. Average temperatures were evaluated using the two approaches mentioned; $\widetilde{T}_{specimen,30}$ and $\widetilde{T}_{specimen,22}$ were found by assessing 30 and 22 layers, respectively. Using the table referenced in

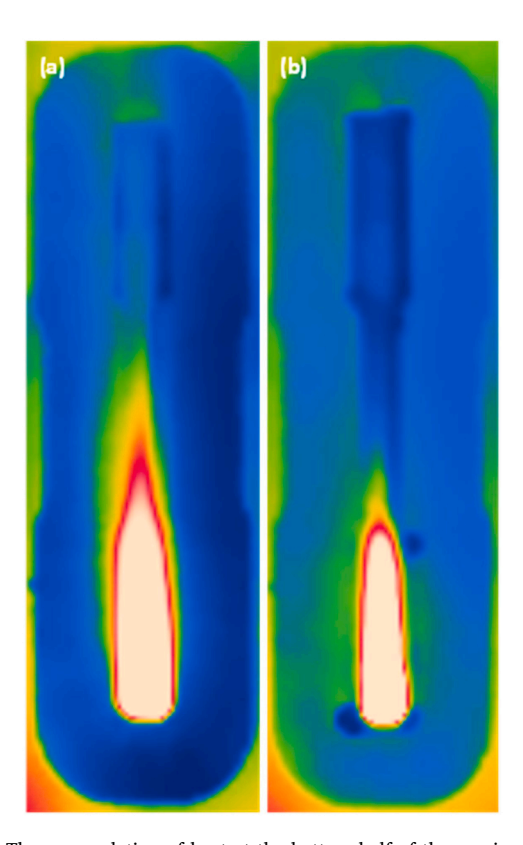


Fig. 11. The accumulation of heat at the bottom half of the specimen due to initial heat transfer to the build plate and extended print durations in (a) layers 4–7 and (b) layer 30–33 of the print leading to an end condition for determination of $\widetilde{T}_{specimen}$.

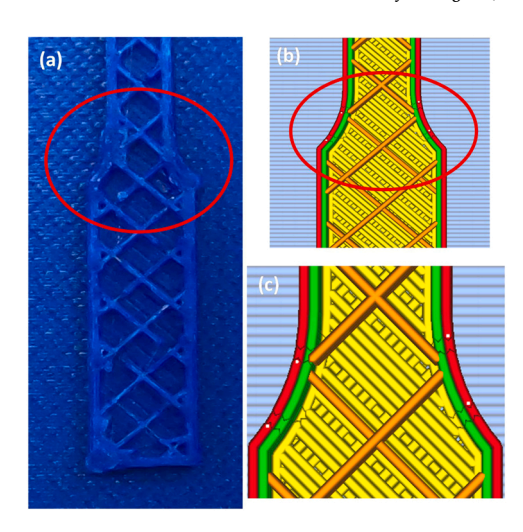


Fig. 12. (a) Over-extrusion and insufficient layer deposition due to the accumulation of point defects at the fillets are visible in optical images and confirmed as (b, c) embedded defects in the sliced layers on Cura.

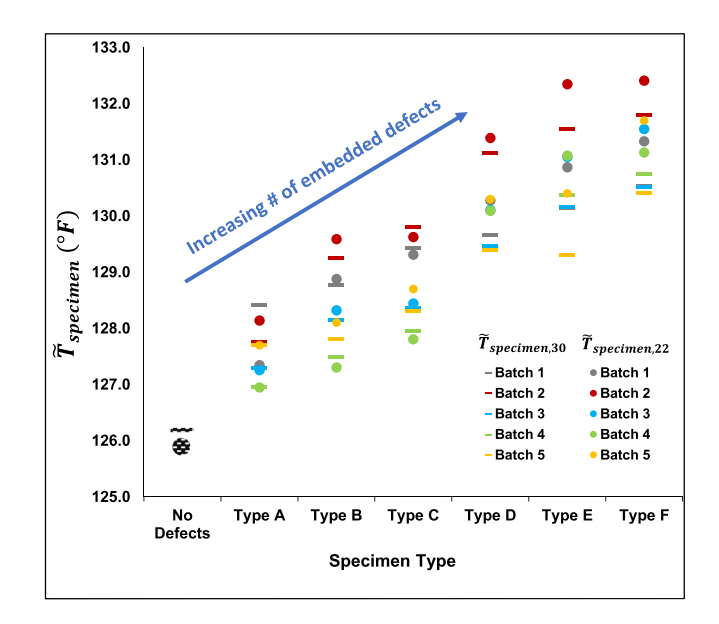


Fig. 13. Average temperatures of printed ASTM test specimens *Types A-F* assessed over 30 and 22 layers for multiple batches of prints showing an increasing $\tilde{T}_{specimen}$ as the number of embedded defects in the specimens increases. A global average temperature of the printed ASTM test specimen with no defects is included for reference.

Task 2 Step 4, a chart was created. Results are pictured in Fig. 13. The average temperature of the print with no defects was determined through extensive experimentation to obtain a global average temperature over 30 and 22 layers, with a standard error (SE) of 0.15°F and a relative standard error (RSE) of 0.12%.

All trials registered similar results. As seen in Fig. 13, $\widetilde{T}_{specimen}$ increased from $Type\ A$ through $Type\ F$ for both approaches used. As the number of embedded defects in the specimen increased, $\widetilde{T}_{specimen}$ also increased. Hence, there exists a positive correlation between $\widetilde{T}_{specimen}$ and the number of embedded defects. For $Types\ A$ through F, $\widetilde{T}_{specimen,30}$ ranged from 127.0°F to 131.8°F, while $\widetilde{T}_{specimen,22}$ ranged from 127.0°F to 132.4°F. A larger variation in temperatures was observed for $\widetilde{T}_{specimen,22}$. The largest increase in $\widetilde{T}_{specimen}$ between any two consecutive types (1.3% or 1.7°F on average) occurred between $Types\ C$ and D.

Fig. 14 shows the total number of spotmeter measurements from

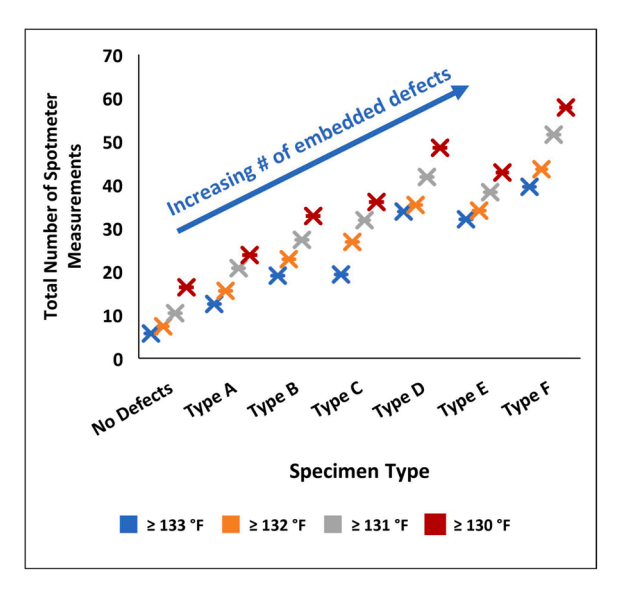


Fig. 14. Total number of spotmeter measurements from Sp1-Sp7 that are greater than or equal to threshold temperature value in 22 layers of *No Defects* and *Types A-F* specimens (average across all trials) showing an increasing number of spotmeter measurements with elevated temperatures as the number of embedded defects increases.

Sp1-Sp7 that are greater than or equal to a threshold temperature value (i.e., 130, 131, 132 or 133°F) in layers 8–29 of the *no defects* and *Types A* through *F* specimens. An average of all trials is presented. It was found that for all threshold temperature values, similar trends were registered: the total number of spotmeter measurements greater than or equal to the specified temperature increased from *No Defects* to *Type A* and from *Types A* to *B, B* to *C, C* to *D,* and *E* to *F,* but decreased slightly from *Type D* to *E.* Nonetheless, there is a positive correlation from *Types A* through *F.* This emphasizes that elevated temperatures are directly correlated to the increasing number of embedded defects in the specimens, specifically point defects.

The greatest increase in spotmeter measurements (75.3%) between two consecutive types occurred between *Types C* to *D* over a threshold of

133°F. The greatest increase in spotmeter measurements for all thresholds (>100%) occurred between *No Defects* and *Type A*. For all trials, $\tilde{T}_{hotspot}$ was greatest for *Type E* (144.67°F) followed by *Type D* (141.89°F) then *Type F* (141.30°F). It was least for *Type A* (139.16°F).

As the number of multilayer defects increased from *Types A* through *F*, the effects of over-extrusion became more evident in the optical images. As observed in Fig. 15, excess material occupied a larger surface area around the fillets as the number of defects increased. As a result, the specimens' boundaries expanded from *Types A* through *F*, and the inner and outer walls became less defined. Through inspection, it was observed that empty infill area around the inner walls became increasingly permeated by excess material as the number of embedded defects increased.

Similarly, at the corners of the geometries, oozing and excess material due to over-extrusion can be clearly identified in the optical images (see Fig. 16a) and verified on the sliced layers (see Fig. 16b).

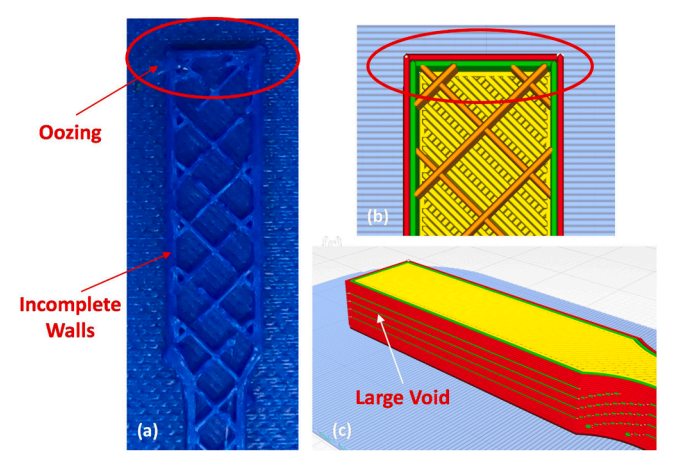


Fig. 16. (a) Incomplete walls due to under-extrusion followed by over-extrusion at the fillet, as well as oozing and accumulation of excess material is observed in an optical image of a layer, (b) point defects at the corners of the specimen leading to the observed defects in a are observed on the same layer in Cura, and (c) isometric view of the specimen on Cura showing a large void that led to the incomplete walls shown in a.

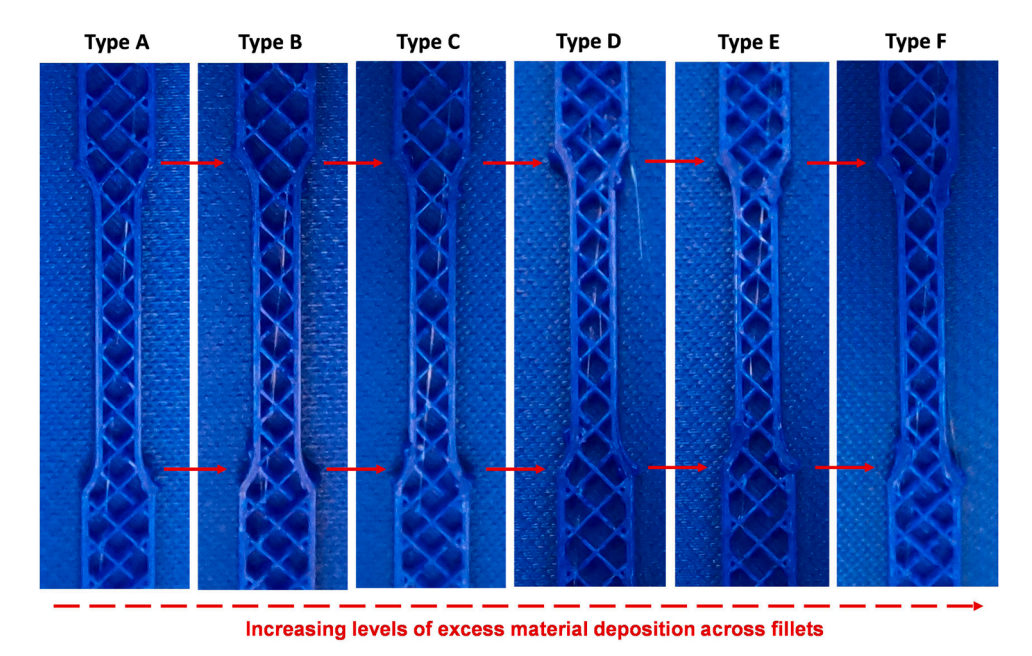


Fig. 15. Optical images of layer 20 for each of *Types A* through *F* showing the increasing levels of over-extrusion or excess material deposition across the fillets due to the accumulation of point defects.

Additionally, as pictured in Fig. 16a, under-extrusion due to a large void (see Fig. 16c) led to incomplete walls at the left edge of the specimen, which is then followed by over-extrusion at Sp2.

Fig. 17 shows optical images of layer 22 of *Types A* and *E* that were processed by applying the *FeatureJ Laplacian* and other image processing algorithms to develop a binary image. Discontinuities in the layer depth along the specimen's boundaries and excess material extrusion at the fillets are apparent in the processed image through the use of the edge detection strategy (see Fig. 17c and d). This is confirmed by applying the same image processing method to an image of the same layer for a specimen with 1/5 of the total embedded defects (see Fig. 17a and b) – *Type E* compared to *Type A*. Processed images can then be compared through evaluation of the specimen's boundaries, where larger perimeters or surface areas are more likely to indicate out-of-control conditions. Area percentage with respect to the number of pixels in a binary image can be compared. This is one example of the use of edge detection filters in ImageJ for the development of a defect detection strategy that can be used in-situ. Other strategies can also be envisioned.

4. Discussion

Optical imaging and image analysis helped in identifying the necessary variables that can lead to real-time defect detection through image correlation. One of many byproducts of defects that were observed in optical images were excess material deposition, both interior and exterior. These instances of over-extrusion were important to note for the purpose of image correlation and assessment of the in-situ monitoring system.

As presented in *Section 3*, excess material surrounding the corners and fillets were observed for all *Types A* through F, where the high spatial resolution of the camera allowed for capturing the expanded walls for all specimen types. The image processing methods allowed to define edges and boundaries and trace perimeters, all of which could be used to quantify the effects of an increasing number of multilayer defects on the surface areas of printed layers. This was demonstrated through the use of edge detection filters for acquiring specimen size information, such as perimeter and surface area. Size information can then be compared for image correlation by referring to a baseline, where larger values are indicative of out-of-control conditions. In this work, out-of-control conditions refer to the formation of embedded defects in the

specimens; however, the aforementioned method can be applied even if the frequency and locations of defects are unknown. Moreover, the results obtained by optical images demonstrate that the algorithm used in this work for embedding random defects can serve as a good measure for validating the effectiveness of an in-situ monitoring system, regardless of defect type or void size.

The results confirmed that sensor characteristics govern the temporal resolution of an in-situ monitoring system, while processing parameters such as layer height, printing speed, and time lapse features govern the frequency of image acquisition needed. Furthermore, the spatial resolution of the monitoring system must be measured to determine its capabilities in detecting embedded defects of different shapes and sizes. In this work, the spatial resolution of the in-situ monitoring system was determined to be $< 1~\rm mm$, which was sufficient for monitoring the FFF process on a bed size of 250 \times 210 mm.

The results emphasize common trends in the datasets. As the number

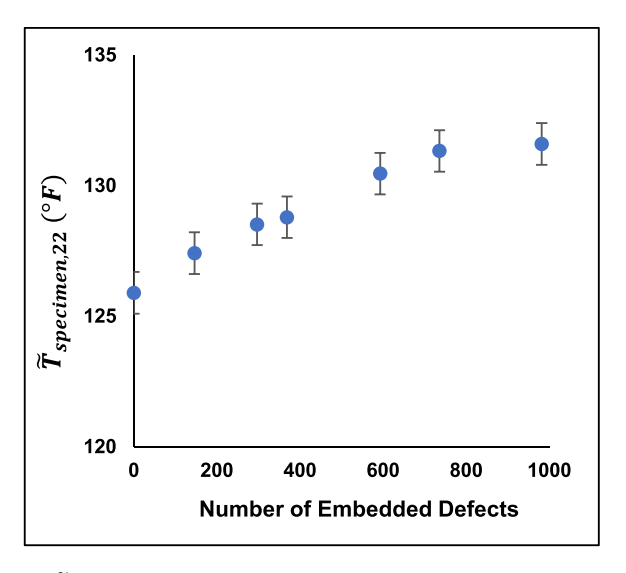


Fig. 18. $\widetilde{T}_{specimen,22}$ vs. the number of embedded defects in a specimen determined through an in-situ defect detection strategy.

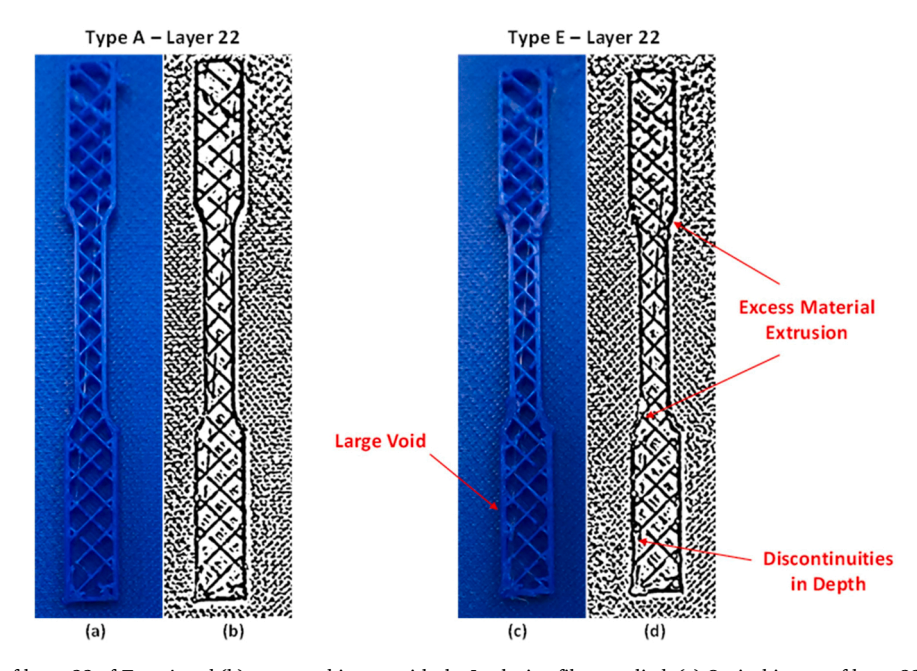


Fig. 17. (a) Optical image of layer 22 of *Type A* and (b) processed image with the Laplacian filter applied. (c) Optical image of layer 22 of *Type E* and (b) processed image with the Laplacian filter applied showing excess material extrusion at the fillets and discontinuities in depth at the boundary due to an embedded line defect.

of embedded defects increased, \tilde{T}_{layer} increased and, hence $\tilde{T}_{specimen}$ also increased. Fig. 18 shows a positive correlation between $\tilde{T}_{specimen,22}$ and the number of embedded defects. The same trend can be seen for $\tilde{T}_{specimen,30}$. Additionally, the accumulation of embedded point and line defects due to delayed extrusions over multiple layers also increased leading to an increasing number of multilayer defects from $Types\ A$ through F. This led to slower cooling rates across the layers due to the entrapment of air in the voids, which resulted in elevated temperature values, specifically at the defined locations Sp1-Sp7. Elevated temperature values were also due to the frequency and sizes of embedded defects in layers 8-29 of the specimens. Moreover, the total number of hotspots at Sp1-Sp7 in each specimen increased over all the printed layers from $Types\ A$ through F. This is directly correlated to an increase in the formation of multilayer defects at the defined locations.

Another trend that was observed in the datasets was the constant increase in average temperatures at each of Sp2-Sp8 from *Types A* through F, which is likely also due to the increasing number of multilayer defects. The average temperature of Sp1 did not fit this trend. As Sp1 represents the starting point of deposition for each layer, it is allowed the most time to cool prior to image acquisition, and thus, average temperatures relative to defect formation may have been affected across all types. There was no correlation found between layer number and \widetilde{T}_{layer} .

The largest increase in $T_{specimen}$ between any two consecutives types (1.3% or 1.7°F on average) occurred between Types C and D. This may be attributed to a large increase in the number of defects between the two types (224). However, this may not be the case as between *Types E* and *F*, there was a large increase in the number of defects (246), but the smallest increase in $\widetilde{T}_{specimen}$ (0.21% or 0.27°F on average). Instead, it is likely due to the large differentiation in the distribution of point and line defects along the specimen's walls for these two types. As the number of embedded defects in Types A through F is dependent on α , the total number of defects at each of Sp1-Sp7 that overlap over successive layers may not consistently increase from Types A through F. Therefore, there may have been a larger increase in the number of multilayer defects from $Type\ C$ to D compared to $Type\ E$ to F, leading to a larger increase in $\widetilde{T}_{specimen}$. Overall, a relationship can be determined between the number of embedded defects and $\widetilde{T}_{specimen}$, as shown in Table 3. An increase in the number of defects by 2X and 5X led to a 2.1% and 4.3% increase in $\widetilde{T}_{specimen}$. With respect to RSE, an increase in the number of defects by 2X and 5X led to a \sim 18X and 37X increase in $\widetilde{T}_{specimen}$, respectively.

The total number of spotmeter measurements from Sp1-Sp7 greater than or equal to a threshold temperature value increased from No Defects to Types A through F for all threshold temperature values (i.e.,130, 131, 132, and 133°F). Considering $\tilde{T}_{specimen,22}$ of 125.9°F for the No Defects specimen, assessing the spotmeter measurements over the different thresholds emphasizes the consistency in the results. The greatest increase in spotmeter measurements (75.3%) between two consecutive types occurred between Types C to D over a threshold of 133°F, which is consistent with the results found for $\tilde{T}_{specimen}$ as mentioned above. The total number of spotmeter measurements decreased slightly from Type D

 $\begin{tabular}{ll} \textbf{Table 3} \\ \textbf{Relationship between the number of embedded defects and percent increase in } \\ \widetilde{T}_{specimen} \end{tabular} \begin{tabular}{ll} \textbf{Y}_{specimen} \end{tabular}$

# of defects	% increase in $\widetilde{T}_{specimen}$	% increase w.r.t. to RSE
0	-	-
у	-	-
2 y	2.1	17.9
2.5 y	2.3	19.7
2 <i>y</i> 2.5 <i>y</i> 4 <i>y</i>	3.6	30.8
5 y	4.3	36.8
6 y	4.5	38.5

to E, which may have been due to a differentiation in the distribution of defects in the specimens allowing a greater number of elevated temperature values to accumulate at the eight locations in $Type\ D$ specimens compared to $Type\ E$ specimens. The greatest increase in spotmeter measurements for all thresholds (>100%) occurred between $No\ Defects$ and $Type\ A$, which asserts that in-situ defect detection can be achieved by assessing spotmeter measurements over a defined threshold and comparing to a baseline. Furthermore, the sum of percentage increases from $No\ Defects$ to $Type\ A$ up through $Type\ F$ was highest for a threshold of $133^{\circ}F$, which emphasizes that the definition of a hotspot stated in $Section\ 2.5.2$ is viable. These trends are emphasized in Fig. 19, where the total number of hotspots is correlated to α . It is apparent that the total number of hotspots increases at a specific rate as α decreases, hence, the correlation can be represented through a power trendline.

For all trials, $\widetilde{T}_{hotspot}$ was greatest for $Type\ E\ (144.67^\circ F)$ followed by $Type\ D\ (141.89^\circ F)$ then $Type\ F\ (141.30^\circ F)$. It was least for $Type\ A\ (139.16^\circ F)$. Therefore, with the exception of $Type\ F$, there is a positive correlation between the global $\widetilde{T}_{hotspot}$ and the total number of embedded defects in the specimen. From $Type\ A$ to $Type\ E$, $\widetilde{T}_{hotspot}$ increased by 4%.

Overall, if the locations of defects were unbeknownst, this in-situ defect detection process would still be applicable, as the process can be repeated for any number of spotmeter temperature measurements per layer. The accuracy of a determined average temperature value for a printed specimen would increase with an increasing number of spotmeter temperature measurements.

5. Conclusions

The multi-sensor in-situ monitoring system introduced in this work allowed for in-situ defect detection through temperature variations monitoring by comparing to a standard baseline. Random embedded defects are observed in Cura to determine an approach for defect detection that can be replicated for other geometries. Compromised AM prints are detected in-situ through the acquired raw dataset by creating a snapshot of temperature variations at a specific time stamp for each layer of the print. It was found that as the number of embedded defects increased in the specimens, $\widetilde{T}_{specimen}$ increased. A positive correlation between the two variables is evident. An increase in the number of defects by 2X and 5X led to a 2.1% and 4.3% increase in $\widetilde{T}_{specimen}$, respectively. With respect to RSE, an increase in the number of defects by 2X and 5X led to a \sim 18X and 37X increase in $\widetilde{T}_{specimen}$, respectively.

Multilayer defects were formed in the specimens due to the accu-

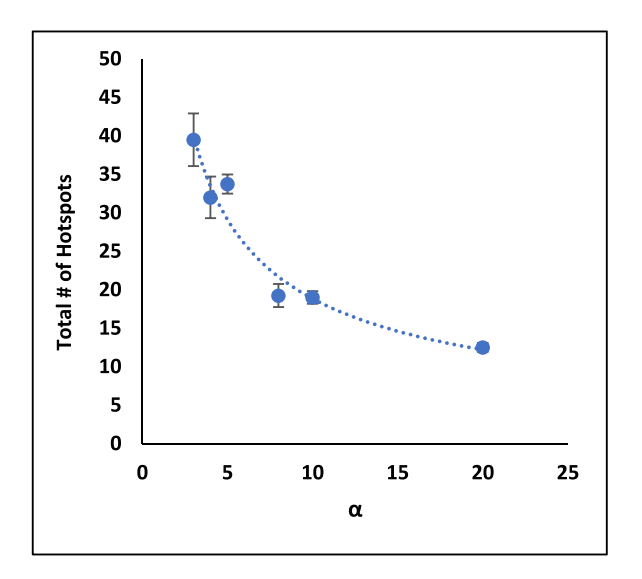


Fig. 19. Total number of hotspots from Sp1-Sp7 vs. the frequency of defect formation, α . A power trendline is used to represent the correlation.

mulation of embedded point and line defects in similar locations on consecutive layers. This led to slower cooling rates across the layers due to the entrapment of air in the voids, resulting in elevated temperature values at the defined locations, as well as an increasing number of spotmeter temperature measurements that were above the threshold temperature values. The greatest increase in spotmeter measurements (75.3%) between two consecutive types occurred between $Types\ C$ to D over a threshold of $133^{\circ}\mathrm{F}$, which is consistent with the results found for $T_{specimen}$. It was also shown that the total number of hotspots increased at a specific rate as α decreased, which was represented through a power trendline. Furthermore, the greatest increases in spotmeter measurements altogether (>100%) occurred between $No\ Defects$ and $Type\ A$, which asserts that in-situ defect detection can be achieved by assessing spotmeter measurements over a defined threshold and comparing to a baseline.

CRediT authorship contribution statement

Conceptualization: Youssef AbouelNour, Nikhil Gupta Formal Analysis: Youssef AbouelNour. Investigation: Youssef AbouelNour. Resources: Youssef AbouelNour. Writing – Original Draft: Youssef AbouelNour. Writing – Review & Editing: Youssef AbouelNour, Nikhil Gupta. Visualization: Youssef AbouelNour, Nikhil Gupta. Supervision: Nikhil Gupta. Project Administration: Nikhil Gupta. Funding Acquisition: Nikhil Gupta.

Declaration of Competing Interest

The authors declare that they have no known competing financial interests or personal relationships that could have appeared to influence the work reported in this paper.

Data Availability

Data will be made available on request.

Acknowledgment

The authors would like to thank Hammond Pearce for his assistance in developing an algorithm for intentional defect formation. Funding for this work is supported by the 2022 American Society of Non-destructive Testing (ASNT) Fellowship Award and the National Science Foundation grant CMMI-2036802. The views expressed in this article are those of the authors and not of the funding agencies.

References

- [1] E.G. Gordeev, A.S. Galushko, V.P. Ananikov, Improvement of quality of 3D printed objects by elimination of microscopic structural defects in fused deposition modelling, PLOS One 13 (6) (2018), e0198370.
- [2] G.L. Chen, K. Yanamandra, N. Gupta, Artificial neural networks framework for detection of defects in 3D-printed fiber reinforcement composites, JOM 73 (2021) 2075–2084
- [3] K. Yanamandra, G.L. Chen, X. Xu, G. Mac, N. Gupta, Reverse engineering of additive manufactured composite part by toolpath reconstruction using imaging and machine learning. Compos. Sci. Technol. 198 (2020), 108318.
- [4] A. du Plessis, S.G. le Roux, J. Els, G. Booysen, D.C. Blaine, Application of microCT to the non-destructive testing of an additive manufactured titanium component, Case Stud. Nondestruct. Test. Eval. 4 (2015) 1–7.
- [5] Y. AbouelNour, N. Gupta, In-situ monitoring of sub-surface and internal defects in additive manufacturing: A review, Mater. Des. 222 (2022), 111063.
- [6] M.R. Khosravani, Z. Bozic, A. Zolfagharian, T. Reinicke, Failure analysis of 3D-printed PLA components: Impact of manufacturing defects and thermal ageing, Eng. Fail. Anal. 136 (2022), 106214.
- [7] C. Oztan, R. Karkkainen, M. Fittipaldi, G. Nygren, L. Roberson, M. Lane, E. Celik, Microstructure and mechanical properties of three dimensional-printed continuous fiber composites. J. Compos. Mater. 53 (2) (2018) 271–280.
- [8] D.V. Betim, M.C. Heymann, O.L.G. Quelhas, R.G.G. Caiado, H.G. Costa, "Analysis of the Application of Additive Manufacturing in the Circular Economy: An Integrative Literature Review," in Operations Management for Social Good, Springer Proceedings for Business and Economics, 2020, pp. 1075–1084.

- [9] X. Yang, D. Zhao-wang, G. Xue-yi, T. Qing-hua, L. Yong, Towards a circular metal additive manufacturing through recycling of materials: A mini revie, J. Cent. South Univ. 27 (2020) 1134–1145.
- [10] Y. Chivel, I. Smurov, On-line temperature monitoring in selective laser sintering/melting, Phys. Procedia 5 (2010) 515–521.
- [11] F. Bayle and M. Doubenskaia, "Selective Laser Melting process monitoring with high speed infra-red camera and pyrometer," in SPIE - The International Society for Optical Engineering, Saint-Etienne, 2008.
- [12] U. Thombansen, A. Gatej, M. Pereira, Process observation in fiber laser-based selective laser melting, pp. 011008-1, Opt. Eng. 54 (1) (2015), pp. 011008-1.
- [13] M. Doubenskaia, M. Pavlov, Y. Chivel, Optical system for on-line monitoring and temperature control in selective laser melting technology (April), Key Eng. Mater. 437 (2010) 458–461 (April).
- [14] S. Liang and J. Wang, "A systematic view of remote sensing," in Advanced Remote Sensing, 2 ed., 2020, pp. 1–57.
- [15] D. Bull and F. Zhang, "Communicating pictures the future," in Intelligent Image and Video Compression, 2 ed., 2021, pp. 485–513.
- [16] A. Gaikwad, B. Giera, G.M. Guss, J.-B. Forien, M.J. Matthews, P. Rao, "Heterogeneous sensing and scientific machine learning for quality assurance in laser powder bed fusion - A single-track study,", Addit. Manuf. vol. 36 (2020), 101659.
- [17] K. Pooladvand, A.D. Salerni and C. Furlong, "In-situ Thermal Monitoring of Printed Components During Rapid Prototyping by Fused Deposition Modeling," in Residual Stress, Thermomechanics & Infrared Imaging and Inverse Problems, vol. 6, 2020, pp. 131–140.
- [18] B. Gould, S. Wolff, N. Parab, C. Zhao, In situ analysis of laser powder bed fusion using simultaneous high-speed infrared and x-ray imaging, JOM J. Miner., Met. Mater. Soc. 73 (1) (2020) 201–211.
- [19] J.L. McNeil, K. Sisco, C. Frederick, M. Massey, K. Carver, F. List III, C. Qui, M. Mader, S. Sundarraj, S. Babu, In-situ monitoring for defect identification in nickel alloy complex geometries fabricated by L-PBF additive manufacturing (October), Metall. Mater. Trans. A 51 (2020) 6528–6545 (October).
- [20] G. Mohr, S.J. Altenburg, A. Ulbricht, P. Heinrich, D. Baum, C. Maierhofer, K. Hilgenberg, In-situ defect detection in laser powder bed fusion by using thermography and optical tomography—comparison to computed tomography, Metals 10 (1) (2020) 103.
- [21] S.M. Estalaki, C.S. Lough, R.G. Landers, E.C. Kinzel, T. Luo, Predicting defects in laser powder bed fusion using in-situ thermal imaging data and machine learning, Addit. Manuf. 58 (2022), 103008.
- [22] J.-B. Forien, N.P. Calta, P.J. DePond, G.M. Guss, T.T. Roehling, M.J. Matthews, Detecting keyhole pore defects and monitoring process signatures during laser powder bed fusion: A correlation between in situ pyrometry and ex situ X-ray radiography, Addit. Manuf. 35 (2020), 101336.
- [23] L. Scime, J. Beuth, Anomaly detection and classification in a laser powder bed additive manufacturing process using a trained computer vision algorithm, Addit. Manuf. 19 (2018) 114-126.
- [24] L. Scime, J. Beuth, Using machine learning to identify in-situ melt pool signatures indicative of flaw formation in a laser powder bed fusion additive manufacturing process. Addit. Manuf. 25 (2019) 151–165.
- [25] L. Pagani, M. Grasso, P.J. Scott, B.M. Colosimo, Automated layerwise detection of geometrical distortions in laser powder bed fusion, Addit. Manuf. 36 (2020), 101435.
- [26] J.A. Mitchell, T.A. Ivanoff, D. Dagel, J.D. Madison, B. Jared, Linking pyrometry to porosity in additively manufactured metals, Addit. Manuf. 31 (100946) (2020).
- [27] Y. Fu, A. Downey, L. Yuan, A. Pratt, Y. Balogun, In situ monitoring for fused filament fabrication process: A review, Addit. Manuf. 38 (2021), 101749.
- [28] D.B. Patil, A. Nigam and S. Mohapatra, An image processing approach to measure features and identify the defects in the laser additive manufactured components," in 2021 4th International Conference on Recent Trends in Computer Science and Technology (ICRTCST), 2022.
- [29] M. Heinl, F.K. Schmitt, T. Hausotte, In-situ contour detection for additive manufactured workpieces, Procedia CIRP 74 (2018) 664–668.
- [30] M. Lerchen, J. Hornung, Y. Zou, T. Hausotte, Methods and procedure of referenced in situ control of lateral contour displacements in additive manufacturing, J. Sens. Sens. Syst. 10 (2021) 219–232.
- [31] A. Ravendran, S. Rianmora, Application of image-based acquisition techniques for additive manufacturing using canny edge detection, J. Comput. Appl. Res. Mech. Eng. 10 (2) (2021) 391–404.
- [32] F. Corradini, M. Silvestri, Design and testing of a digital twin for monitoring and quality assessment of material extrusion process, Addit. Manuf. 51 (2022), 102633.
- [33] A. Cano-Vicent, M.M. Tambuwala, S.S. Hassan, D. Barh, A.A.A. Aljabali, M. Birkett, A. Arjunan, A. Serrano-Aroca, Fused deposition modelling: Current status, methodology, applications and future prospects, Addit. Manuf. 47 (2021), 102378.
- [34] C. Liu, A.C.C. Law, D. Roberson, Z. Kong, Image analysis-based closed loop quality control for additive manufacturing with fused filament fabrication, J. Manuf. Syst. 51 (2019) 75–86.
- [35] D.A. Brion, M. Shen, S.W. Pattinson, Automated recognition and correction of warp deformation in extrusion additive manufacturing, Addit. Manuf. 56 (2022), 102838.
- [36] R.-E.-N. Hossain, J. Lewis, A.L. Moore, In-situ infrared thermal temperature sensing for real-time defect detection in additive manufacturing, Addit. Manuf. 47 (2021), 102328.
- [37] M. Grasso, A. Demir, B. Previtali, B. Colosimo, In situ monitoring of selective laser melting of zinc powder via infrared imaging of the process plume, Robot. Comput. -Integr. Manuf. 49 (2018) 229–239.

- [38] B. Wijnen, P. Sanders, J.M. Pearce, "Improved model and experimental validation of deformation in fused filament fabrication of polylactic acid,", Prog. Addit. Manuf. vol. 3 (2018) 193–203.
- [39] "ImageJ," National Institutes of Health.
- [40] S. Uchida, Image processing and recognition for biological images, Dev. Growth Differ. 55 (2013) 523–549.
- [41] J. Canny, A computational approach to edge detection, IEEE Trans. Pattern Anal. Mach. Intell. PAMI-8 (6) (1986) 679–698.
- [42] L. Yuan , X. Xu, "Adaptive Image Edge Detection Algorithm Based on Canny Operator," in 2015 4th International Conference on Advanced Information Technology and Sensor Application (AITS), Harbin, China, 2015.
- [43] J.W. Woods, Image enhancement and analysisin. Multidimensional Signal Image, and Video Processing and Coding, 2 ed., Academic Press, 2012, pp. 223–256.
- [44] E. Meijering, "FeatureJ: An ImageJ Plugin Suite for Image Feature Extraction," imagescience.org. [Online]. [Accessed 2022].
- [45] R. Guo, Z. Ren, H. Bi, M. Xu, L. Cai, Electrical and thermal conductivity of polylactic acid (PLA)-based biocomposites by incorporation of nano-graphite fabricated with fused deposition modeling, Polymers 11 (3) (2022) 549.